ACS Catalysis

pubs.acs.org/acscatalysis

Research Article

Contrasting Arene, Alkene, Diene, and Formaldehyde Hydrogenation in H-ZSM-5, H-SSZ-13, and H-SAPO-34 Frameworks during MTO

Mykela DeLuca, Christina Janes, and David Hibbitts*

Cite This: *ACS Catal.* 2020, 10, 4593−4607

Read Online

ACCESS | Metrics & More | Article Recommendations | Supporting Information

ABSTRACT: Co-feeding H_2 at high pressures increases zeolite catalyst lifetimes during methanol-to-olefin (MTO) reactions while maintaining high alkene-to-alkane ratios; however, the atomistic mechanisms and species hydrogenated by H_2 co-feeds to prevent catalyst deactivation remain undetermined. This study uses periodic density functional theory (DFT) to examine mechanisms and rates of hydrogenating MTO product alkenes and species formed during MTO that have been linked to catalyst deactivation: C_4 and C_6 dienes, formaldehyde, and benzene. Hydrogenations of these species are examined in models of H-ZSM-5 (MFI framework), H-SSZ-13 and H-SAPO-34 (CHA framework). Single-step and two-step hydrogenation mechanisms occur with similar barriers for all reactants on all zeolites, with H_2 dissociation (hydride transfer) being the difficult part of these mechanisms. Hydrogenation barriers trend well with carbenium stabilities, and species that form oxocarbeniums or allylic carbocations hydrogenate at higher rates than those proceeding via alkylcarbeniums. As such, dienes and formaldehyde are selectively hydrogenated during MTO compared to alkenes, occurring with barriers 10−85 kJ mol^{-1} lower than C_2−C_4 alkene hydrogenation, with formalde hydehydrogenation on average 10 kJ mol^{-1} lower than diene hydrogenation. Butadiene hydrogenation is also facilitated by α,δ protonation and hydridation schemes, which form 2-butene as primary products, in contrast to α,β routes forming 1-butene—both routes occur via allylic carbocations, indicating that carbocation stability is not the only driver towards selective diene hydrogenation. Barriers of hexadiene hydrogenation are lower than those of butadiene, indicating that longer carbon chains can stabilize the intermediate carbocations. Benzene, in contrast to dienes and formaldehyde, is hydrogenated with higher barriers than C_2−C_4 alkenes despite proceeding via stable benzenium cations because of the instability of the nonaromatic product. Hydrogenation barriers in H-SSZ-13 and H-ZSM-5 are within 12 kJ mol^{-1} of one another indicating both demonstrate similar hydrogenation rates. Hydrogenation barriers in H-SAPO-34 are 12−38 kJ mol^{-1} higher than those in H-SSZ-13 (both CHA) and the SAPO zeotype also seems to favor formaldehyde hydrogenation over diene hydrogenation (in contrast to the aluminosilicates). H_2O increases the efficacy of H_2 co-feeds but does not directly assist in hydrogenation pathways; instead, it increases hydrogenation rates by increasing the concentration of surface protons through alkyl hydration reactions.

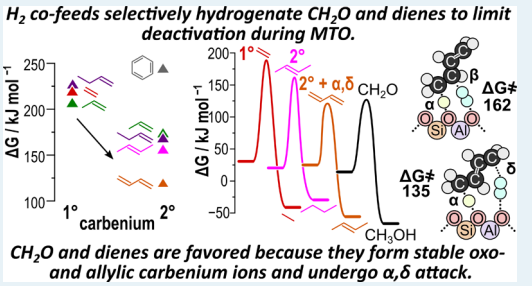

KEYWORDS: *hydrogenation, methanol-to-olefins, deactivation, zeolites, Brønsted acid catalysis*

1. INTRODUCTION

Zeolite-catalyzed methanol-to-olefin (MTO) reactions are a widely studied[1−7] alternative route for producing light olefins, primarily C_2−C_4 alkenes. Zeolite catalysts, however, are susceptible to deactivation via the formation of large, polyaromatic species, thus limiting their efficiency and requiring the use of recirculating fluidized bed reactors in industrial applications.[8−13] During MTO, alkenes are formed in two complementary co-catalyzed cycles: the aromatic cycle and the olefin cycle (Scheme 1).[14−19] In the olefin cycle, alkenes methylate and grow to a size capable of cracking into C_3−C_5 compounds.[1,17,20,21] These olefins can undergo hydride transfer reactions to form alkanes and dienes—either via alkene disproportionation[22,23] or (more likely) through formaldehyde (CH_2O)-assisted[24−26] routes—which can cyclize to form aromatic species.[27−29] Aromatics can undergo isomerization and dealkylation to further co-catalyze the formation of alkenes in the aromatics cycle.[1,16,30−32] Aromatic species can also react with dienes to form site-blocking polyaromatic species,[11,33−36] which ultimately deactivate the catalyst.[12] Therefore, CH_2O and dienes play a critical role in

Received: October 20, 2019
Revised: March 9, 2020
Published: March 10, 2020

https://dx.doi.org/10.1021/acscatal.9b04529
ACS Catal. 2020, 10, 4593−4607

Scheme 1. Dual Cycle Mechanism of MTO Chemistry[a]

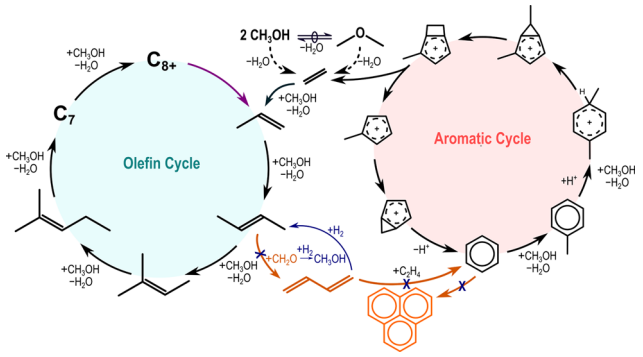

[a]Orange reactions depict deactivating mechanisms during MTO, which are prevented by reaction with H_2 to form nondeactivating species, shown in blue.

Scheme 2. Brønsted Acid-Catalyzed Double-Bond Hydrogenation[a]

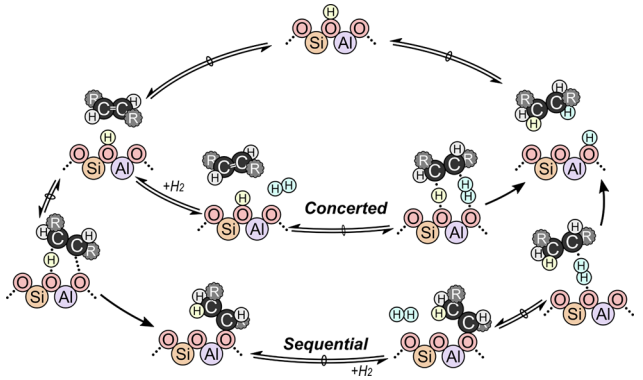

[a]Hydrogenation occur via a concerted single-step pathway or via a two-step sequential pathway, both of which exchange a surface proton with a proton atom derived from H_2, indicating that these pathways cannot be distinguished by isotopic tracer studies.

both the formation of aromatic co-catalysts and deactivation via polyaromatic species.[13]

High-pressure H_2 co-feeds significantly improve catalyst lifetime in common MTO zeolites and zeotypes such as H-SAPO-34, H-SSZ-13 (both the CHA framework) and H-ZSM-5 (MFI framework).[37,38] Co-feeding H_2 at high partial pressures (4−30 bar H_2, 0.13 bar CH_3OH, 673 K) improved the catalyst lifetime, as measured by the turnover number, by a factor of 3−70 in H-SAPO-34. Similarly, H_2 co-feeds at pressures of 0.4 bar in H-SSZ-13 and 16 bar in H-ZSM-5, H-SSZ-39 (AEI framework), H-FER, and H-BEA improved the catalyst lifetime by factors of 3−15.[39] These extensions in the catalyst lifetime did not result in dramatic changes in selectivity; while the alkane-to-alkene ratios generally increased, the predominant C_2−C_3 products remained as alkenes. The observed increases in C_2−C_4 alkane ratios are dependent on zeolite topology. For instance, C_2−C_4 alkane selectivity increases equally in H-CHA, H-BEA, and H-FER (16 bar H_2); however, propane selectivity is higher than that of C_2 and C_4 alkanes in H-AEI, indicating that zeolite topology plays a role in hydrogenation selectivities. The observed increases in catalyst lifetime likely occur because H_2 selectively hydrogenates reactive species that lead to deactivation (i.e., dienes and formaldehyde), thereby limiting the amount of polyaromatic species formed during MTO (Scheme 1). Kinetic studies of alkene and diene hydrogenation in CHA, FER, BEA, and AEI (0.1−1 mbar hydrocarbon, 1−16 bar H_2, 623 K) corroborate the selective hydrogenation of dienes over alkenes by demonstrating that rate constants of butadiene (C_4H_6) hydrogenation are 7−300× larger than those for ethene (C_2H_4) and propene (C_3H_6) in all frameworks.

Catalyst lifetimes can be further improved by combining high-pressure co-feeds of H_2 and H_2O, which prolong the lifetime (as measured by methanol conversion dropping below 80%) of H-SAPO-34 from 75 h with co-fed H_2 (4.2 bar CH_3OH, 35.7 bar H_2, 723 K) to 118 h with co-fed H_2 and H_2O (4.2 bar CH_3OH, 22.8 bar H_2, 12.8 bar H_2O, 723 K).[38] H_2O can assist in mitigating deactivation by increasing the surface coverage of protons (necessary for hydrogenation) by hydration of surface alkyl species (such as CH_3−Z) or by facilitating the protonation of dienes or formaldehyde through direct participaton in hydrogenation steps.

There are two proposed mechanisms of Brønsted acid-catalyzed double-bond hydrogenation[40,41] (Scheme 2): a concerted mechanism in which protonation of the double bond and cleavage of the H−H bond occur simultaneously

$$C_xH_{2x} + H_2 + Z{-}H \rightarrow C_xH_{2x+2} + Z{-}H \quad (1)$$

and a sequential mechanism in which a surface-bound alkyl species is first formed

$$C_xH_{2x} + Z{-}H \rightarrow Z{-}C_xH_{2x+1} \quad (2)$$

followed by subsequent hydridation, or addition of a hydride, by H_2.[41,42]

$$Z{-}C_xH_{2x+1} + H_2 \rightarrow C_xH_{2x+2} + Z{-}H \quad (3)$$

These mechanisms involve the heterolytic splitting of H_2 to transfer a hydride to an organic cation and a proton back to the catalyst surface; thus, isotopic tracer experiments are incapable of distinguishing these mechanisms. Moreover, both mechanisms may have similar kinetic isotope effects (KIEs) if H_2 splitting is the kinetically relevant transition state in both mechanisms. Despite the lack of detailed mechanistic studies, there have been investigations comparing the hydrogenation barriers of different species. These reactions, in the case of alkenes, are the microscopic reverse of dehydrogenation reactions, which are a portion of acid-catalyzed alkane cracking (causing a mixture of dehydrogenation and C−C bond cleavage).[43−46] Previous reports investigating rates of C_3−C_6 cracking and dehydrogenation over H-ZSM-5 and H−Y zeolites have demonstrated that the apparent energies of activation and the rates of hydrogenation are directly proportional to the carbon-chain length.[44] Previous density functional theory (DFT) calculations on 3T cluster models examining hydrogenation of C_2H_4 and CH_2O suggest that in the sequential mechanism, barriers of Z−C_2H_5 formation (eq 2) are facile compared to its hydridation—indicating that the second step (heterolytic H_2 cleavage, eq 3) is kinetically relevant in the sequential mechanism.[42] Overall barriers (relative to the Z−H state) of concerted and sequential hydrogenation are less than 10 kJ mol^{-1} different for ethene,[42] indicating that the two mechanisms are likely competitive; however, these conclusions cannot be extrapolated to larger alkenes and dienes. The overall potential energy barriers of CH_2O hydrogenation are facile (60 kJ mol^{-1}) and are over 100 kJ mol^{-1} lower than those of ethene. CH_2O, formed in situ via

https://dx.doi.org/10.1021/acscatal.9b04529
ACS Catal. 2020, 10, 4593−4607

methanol disproportionation[26] or co-fed,[47] have been shown to react with olefins to increase the selectivity towards dienes and aromatic species.[8,26,47,48] Co-feeding formaldehyde-scavenging Y_2O_3 can slow catalyst deactivation,[49] demonstrating its critical role in decreasing catalyst lifetime. As such, hydrogenation of CH_2O[42] may contribute to the experimentally observed increases in catalyst lifetime.

The increases in the catalyst lifetime observed by the previously discussed kinetic studies[37−39] have demonstrated that hydrogenation reactions play an important role in increasing the catalyst lifetime in zeolites of varying topologies. No theoretical study, however, has investigated and compared hydrogenation mechanisms across multiple alkenes, dienes, aldehydes, and arenes. Such theoretical analysis can provide insight inaccessible by experiments, such as contrasting mechanisms and assessing primary products, to improve our understanding of how H_2 elongates catalyst lifetime and alters the hydrocarbon pool or product selectivity in MTO reactions. Here, we use DFT to examine concerted and sequential (Scheme 1) hydrogenation schemes of C_2−C_4 alkenes, C_4 and C_6 dienes, CH_2O, and benzene. We carry out these reactions in two common MTO zeolite frameworks: MFI and CHA, with the latter being modeled as an aluminosilicate, H-SSZ-13, and a phosphoaluminosilicate, H-SAPO-34. We show hydrogenation of dienes and CH_2O are kinetically favored over alkenes and benzene in all three catalysts, suggesting that elongation of catalyst lifetime can be attributed to elimination of dienes (as CH_2O is a diene precursor). Furthermore, these results indicate that diene hydrogenation preferentially occurs through protonation and hydridation of α,δ (1,4) C-atoms to form 2-butene from butadiene and 3-hexene from 2,4-hexadiene. This α,δ reaction mechanism is more facile than other reactions that similarly proceed through an allylic carbocation, such as α,β hydrogenation of butadiene, indicating that the kinetic benefit of diene hydrogenation is not solely attributable to carbocation stability. Free-energy barriers in aluminosilicate materials (H-ZSM-5 (MFI) and H-SSZ-13 (CHA)) are consistently lower than barriers in the phosphoaluminosilicate material examined (H-SAPO-34)—indicating that frameworks containing stronger acids facilitate hydrogenation better than those with weaker acids. Despite the differences in overall barriers, trends in hydrogenation barriers tend to remain consistent across all three catalysts tested and barriers of butadiene and CH_2O are consistently lower than those of alkenes and aromatics—indicating that the mechanism of lifetime elongation does not significantly change based on catalyst selection.

2. METHODS

2.1. Computational Methods. Periodic, dispersion-corrected density functional theory (DFT) calculations were carried out using the Vienna ab initio simulation package (VASP)[50−53] as implemented in the computational catalysis interface (CCI).[54] Plane waves were constructed using the projector augmented-wave (PAW) potentials with an energy cutoff of 400 eV. The Perdew−Burke−Ernzerhof (PBE) form of the generalized gradient approximation (GGA) was used to determine exchange and correlation energies.[55−57] The DFT-D3 method with Becke and Johnson damping accounted for dispersive interactions.[58−60] The Brillouin zone was sampled at the Γ-point for all calculations.[61] Previous work benchmarking the accuracy of different DFT functionals has demonstrated that PBE-D3 underestimates the activation barriers for methanol dehydrogenation and other reactions (relative to CCSD(T) methods) and that these errors can be limited by employing higher-level calculations such as M06 which decreases the errors to ∼7 kJ mol^{-1}.[62] However, this work focuses on comparing the trends in energy barriers, rather than comparing DFT-obtained energy barriers directly to experimental results or higher-level methods. To confirm that these trends are not dependent on the choice of functional, transition states were also examined using the Bayesian error estimation functional (BEEF)-van der Waals (vdw) functional (Figure S8), and the trends remain the same regardless of functional choice—thus, the remainder of this paper will discuss our results with PBE-D3.

The MFI structure obtained from the experimental results of van Koningsveld et al.[63] is used in all MFI calculations because restructuring artifacts are minimized in this zeolite form (Figure S1).[64] The lattice parameters (a = 20.090 Å, b = 19.738 Å, c = 13.142 Å) and orthorhombic shape were fixed in all calculations. All calculations in MFI were performed with a single Brønsted acid site (Si/Al of 95) at the T11 tetrahedral site (T-site), which has been predicted to have lower CH_3−Z formation barriers than other T-sites residing in the channel intersection (T3, T10, and T12).[65] There are four O-sites surrounding T11: O14, O16, O24, and O25. Previous work has demonstrated that O24 is inaccessible to species larger than CH_3−Z, because of confinement by the surrounding framework;[66] therefore, reactions were investigated at O14, O16, and O25, and their respective combinations for reactions involving two O atoms. The CHA structure (Figure S2) was obtained from the International Zeolite Association (IZA) database—no significant restructuring artifacts are observed upon annealing or optimization of the CHA structure.[64] The lattice parameters ($a = b$ = 13.675 Å, c = 16.675 Å and $\alpha = \beta$ = 90°, γ = 120°) were fixed in all calculations. All reactions in CHA were performed with a single Brønsted acid site at the single crystographically unique T-site of CHA corresponding to a Si/Al ratio of 35. All four O-sites surrounding that T-site were considered for all reactions (and in all combinations for sites that directly interact with a pair of O atoms). The H-SAPO-34 (Figure S3) lattice parameters (a = 13.8704, b = 13.8733, c = 14.9725, α = 90.02, β = 89.99, γ = 119.98) and atomic positions were optimized using an 800 eV energy cutoff so that energies between iterations differed by $<1 \times 10^{-6}$ eV. H-SAPO-34 was modeled with a single Si atom, corresponding to an Al + P/Si ratio of 35 (thus having the same site density as the H-SSZ-13 model).

Reactants, products, and adsorbed intermediates were optimized until the maximum force on any atom was <0.05 eV $Å^{-1}$ in a two-step convergence procedure as implemented in CCI.[54] In the first step, wave functions were converged to within 10^{-4} eV and forces were computed using a fast Fourier transform (FFT) grid with a cutoff 1.5× the plane-wave cutoff. In the second step, accuracy was improved by converging wave functions to within 10^{-6} eV and using an FFT grid 2× the plane-wave cutoff. Critical transition states were also converged so that the maximum force on any atom was <0.01 eV $Å^{-1}$ in a three-step convergence procedure, and the tighter convergence criteria do not have any impact on free-energy trends (Figure S4). No atoms were constrained in any DFT optimization, pathway, or transition-state calculations. Minimum energy pathways were estimated using the nudged elastic band (NEB) method[67] involving 12−16 images and wave functions converged to 10^{-4} eV with an FFT grid 1.5× the size of the

https://dx.doi.org/10.1021/acscatal.9b04529
ACS Catal. 2020, 10, 4593−4607

plane-wave cutoff. The maximum force on each atom in all images was converged to <0.5 eV $Å^{-1}$ for NEB calculations. This estimate of the minimum energy pathway was used to generate initial transition-state structures and reaction modes for the Dimer method,[68] which optimizes a pair of structures to determine the local curvature of the potential energy surface until ultimately converging on a saddle point. Dimer calculations were done in an analogous two-step optimization procedure using the same convergence criteria as reactant, product, and intermediate optimizations. All DFT-optimized reactant, product, and transition states were modeled at all relevant O-sites and O-site pairs (if the species interacted with a pair of O atoms) associated with T11 of MFI and T1 of CHA. Furthermore, all structures were systematically reoriented (Section 2.2),[66] to increase the likelihood that global minima and optimum transition-state structures were obtained via static (non-dynamic) DFT calculations. Converged NEB and dimers in the H-SSZ-13 framework (aluminosilicate CHA framework, Section 3.3) were transferred to the H-SAPO-34 framework (phosphoaluminosilicate CHA framework) using CCI tools, as described in our recent manuscript.[54]

Frequencies were calculated for all reactant, product, and transition states using a fixed displacement method where the adsorbates (e.g., CH_3OH and benzene) and AlO_4 of the acid site are displaced while all other framework atoms are fixed. Low-frequency modes (<60 cm^{-1}) were replaced with 60 cm^{-1} (Table S1), similar to previous work,[65,69] because low frequencies are inaccurate and contribute significantly to vibrational entropy terms. These frequency calculations are used to determine zero-point vibrational energies and vibrational enthalpies and entropies, which can be combined with ideal gas treatments of rotational and translational modes (for bulk gas species) to determine temperature-corrected (353−673 K) enthalpies and free energies using the equations given in Section S3 of the Supporting Information (SI).

2.2. Reorientation of Reactant, Product, and Transition-State Species. All reactant, product, and transition-state structures were modeled on the three accessible O-sites of T11 in MFI (O14, O16, and O24) and at all four unique O-sites in CHA (O1, O2, O3, and O4). Each reactant, product, and transition-state structure was systematically reoriented as implemented in CCI[54] in an attempt to identify the global minimum, rather than local minima. These reorientations can find configurations of guest species with energies as much as 50 kJ mol^{-1} lower than initial user guess, as discussed in previous work,[66] and are often neglected in studies that aim to improve accuracy with higher-level methods.

Reorientation schemes are based on how an adsorbate interacts with the zeolite framework. States that interact non-specifically with the Brønsted acid site (e.g., adsorbed alkenes, dienes, and protonated states) are reoriented in space about the axes defined by the *a*-, *b*-, and *c*-vectors of the unit cell around their centers of mass (Figure 1a). The orientation of each state was varied in 30° increments from 30 to 330° around each of these rotational axes individually and subsequently optimized with the parameters discussed in Section 2.1 to identify the lowest energy orientation.

States that interact strongly with the framework—via covalent, incipient, or hydrogen bonds—are reoriented about the acid site. Three types of acid site reorientations are used here: O_t−Al−Si−O_a (Figure 1b), Al−O_a−A_1, and O_t−O_a−A_1−A_2, which have been described in previous literature.[66] Reorientations about the O_t−Al−Si−O_a dihedral angle sweep

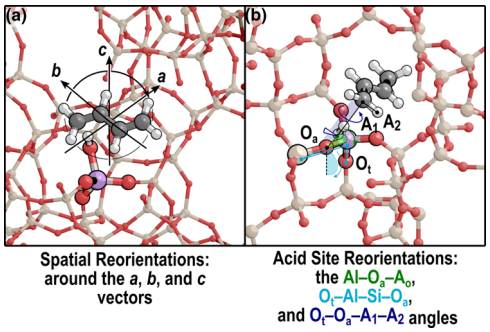

Figure 1. (a) Spatial reorientations of butadiene about the *a*-, *b*-, and *c*-axes of the unit cell and (b) acid site reorientations of the hydrogenation of C_4H_6 (transition state) about the Al−O_a−A_1 angle (green), O_t−Al−Si−O_a angle (cyan), and O_t−O_a−A_1−A_2 (blue).

the adsorbate around the Brønsted acid site (Figure 1b). The orientations of these states were varied in 30° increments from 30 to 330° and all converged states were subsequently optimized. Altering the Al−O_a−A_1 angle moves the adsorbed state parallel to the acid site through the zeolite void (Figure 1b). Each state was reoriented in 15° increments between −30 and 30°, and the four resulting states were reoptimized using the parameters discussed in Section 2.1. Finally, O_t−O_a−A_1−A_2 reorientations result in guest species spun about their interaction with the O atom, with which they interact on the acid site or its conjugate base (Figure 1b). These O_t−O_a−A_1−A_2 reorientations were done in 30° increments from 30 to 330°. Reactant and product states that are covalently bound to the zeolite surface (e.g., C_2H_5−Z) are reoriented with O_t−Al−Si−O_a and O_t−Al−Si−O_a reorientations (covalently bound states are ineligible for Al−O_a−A_1 reorientations) to probe the potential energy surface. States that are not covalently bound but strongly interact with the surface through either hydrogen bonding (e.g., CH_2O) or nascent bonds (e.g., sequential hydrogenation) are rotated through all acid site reorientation schemes.

The alkoxide-forming transition state (eq 2) and the concerted hydrogenation transition state (eq 1) strongly interact with two O-sites simultaneously. Therefore, reorientations of these states would significantly change the transition-state structure, and, as such, these states are not systematically reoriented. However, each transition state was examined between all possible O-site combinations among the 3 accessible O-sites in MFI and 4 accessible O-sites in CHA, resulting in 6 optimized structures for these transition states in MFI and 10 optimized transition states in CHA.

3. RESULTS AND DISCUSSION

3.1. Hydrogenation Thermodynamics. Hydrogenation reactions were investigated for all possible hydrogenation products of ethene, propene, 1-butene, 2-butene, isobutene, butadiene, 2,4-hexadiene, formaldehyde, and benzene (Figure 2). Gas-phase reaction energies (Figure 2) indicate that there is no significant thermodynamic preference to hydrogenate species involved in polyaromatic formation (aromatics, dienes, and formaldehyde) compared to alkenes, and that C=C bond stability increases with C-atom substitution. Trends observed in the DFT-obtained gas-phase hydrogenation enthalpies of the reaction match those obtained experimentally (298 and 355 K)[70,71] for ethene, propene, 1-butene, and 2-butene—both indicating that enthalpies of reactions trend ethene < propene

https://dx.doi.org/10.1021/acscatal.9b04529
ACS Catal. 2020, 10, 4593−4607

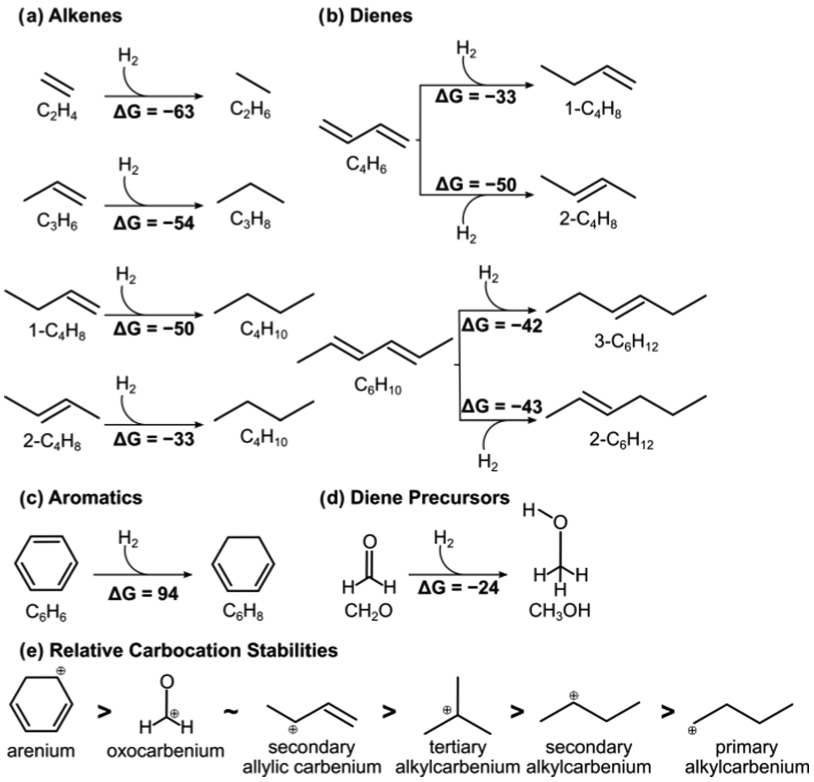

Figure 2. Gas-phase reaction energies of (a) alkene hydrogenation, (b) diene hydrogenation, (c) aromatic hydrogenation, (d) formaldehyde hydrogenation, and (e) relative carbocation stabilities. Free-energy (ΔG) values are reported in kJ mol^{-1} at 623 K.

~ 1-butene < 2-butene (Table S2). This indicates that the tendency for dienes to be hydrogenated over alkenes—as shown experimentally[39]—arises from a kinetic preference, likely because of the resonance-stabilized allylic carbocations that mediate some diene hydrogenation pathways. A preference for formaldehyde hydrogenation over alkene hydrogenation has not been directly observed but has been predicted by DFT calculations contrasting formaldehyde and ethene hydrogenation and demonstrating that the former is stabilized by the formation of oxocarbenium ions.[42] Despite the stability of the benzenium ($C_6H_7^+$) cation, the disruption of the aromaticity results in a large reaction free energy (+94 kJ mol^{-1}) and the instability of the cyclohexadiene product is likely to limit benzene hydrogenation rates. Direct analysis of both hydrogenation mechanisms (sequential and concerted) and altering which carbon is protonated and which is hydridated during these reactions will give additional insights.

3.2. Hydrogenation in H-MFI. Two hydrogenation schemes were considered in this work: a concerted mechanism in which protonation and hydridation occur simultaneously and a sequential mechanism in which the alkene is protonated and forms a zeolite-bound intermediate followed by hydridation by H_2. These mechanisms were investigated for all reactants, except benzene and hexadiene, where only the concerted mechanism was considered because of the similarity between concerted and sequential transition states and the relative difficulty of forming surface-bound C_6 species.

Sequential hydrogenation generally involves the formation of a surface-bound species (C_2H_5−Z for ethene) followed by subsequent hydridation by H_2. Formation of C_2H_5−Z involves simultaneous protonation of the α carbon and C−O bond formation with the β carbon (Figure 3a). The transition state with the lowest energy among all six distinct O-site pair

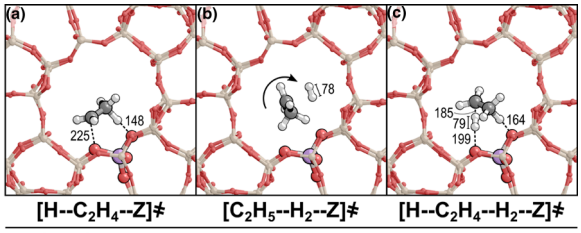

	[H--C_2H_4--Z]‡	[C_2H_5--H_2--Z]‡	[H--C_2H_4--H_2--Z]‡
ΔH‡ (ΔH_{act})	20 (65)	73 (153)	56 (100)
ΔS‡ (ΔS_{act})	−159 (−43)	−236 (−8)	−264 (−65)
ΔG‡ (ΔG_{act})	118 (92)	220 (158)	220 (141)

Figure 3. Transition-state structures of (a) C_2H_5−Z formation, (b) alkoxide hydridation, and (c) concerted hydrogenation in MFI. Enthalpy (H, kJ mol^{-1}), entropy (S, J mol^{-1} K^{-1}) and free-energy (G, kJ mol^{-1}) barriers are reported at 623 K and 1 bar; bond distances are reported in pm. Effective barriers (referenced to gas-phase species and a bare proton, $\Delta G^{\ddagger}$) and intrinsic barriers (in parentheses, ΔG_{act}) are both listed. Transition states for C_3−C_6 species are shown in Section S8 of the Supporting Information.

possibilities is shown in Figure 3a, and the effective free-energy barrier to form this transition state (relative to gas-phase species and a bare proton) is 118 kJ mol^{-1}, with an intrinsic barrier of 92 kJ mol^{-1} (Figure 4). The second step of the sequential mechanism involves detachment and rotation of $C_2H_5^+$ so that heterolytic H_2 dissociation can occur (Figure 3b) to transfer a hydride to the carbocation and a proton to the zeolite surface and occurs with an effective free-energy barrier of 220 kJ mol^{-1}. The free-energy barriers of the two sequential hydrogenation steps (118 and 220 kJ mol^{-1}) cannot be directly compared to evaluate their relative rates because the second step requires H_2 adsorption, and hence the pressure dependences in their respective rate equations differ

https://dx.doi.org/10.1021/acscatal.9b04529
ACS Catal. 2020, 10, 4593−4607

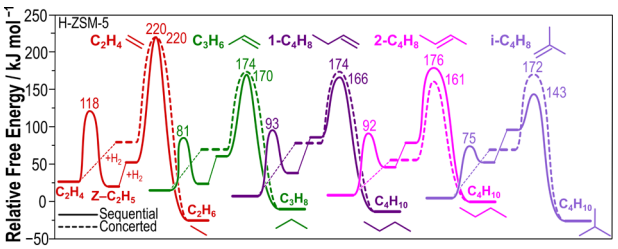

Figure 4. Reaction coordinate diagram of ethene (red), propene (green), 1-butene (dark purple), 2-butene (pink), and isobutene (light purple) concerted (dashed) and sequential (solid) hydrogenation routes. Free energies (kJ mol^{-1}) are reported at 623 K and 1 bar of each alkene and 1 bar H_2. All enthalpy, entropy, and free-energy barriers are reported in Table S6 and transition-state structures are shown in Section S8.

$$\frac{r_{S1}}{[L]} = K_{C_2H_4} k_{S1}(C_2H_4)[*] \quad (4)$$

$$\frac{r_{S2}}{[L]} = K_{C_2H_4} K_{C_2H_4\cdots H_2} K_{S1} k_{S2}(C_2H_4)(H_2)[*] \quad (5)$$

with rate and equilibrium constants being defined in Section S5 of the SI, [L] representing all possible sites, and [*] indicating a bare proton on the zeolite surface. Bare protons (*) will not be abundant at MTO conditions. However, surface methoxies or other species will equally inhibit the rates of both steps (and equally inhibit all reactions studied in this work); therefore, the presence or absence of site-blocking intermediates can be neglected in the analysis of relative hydrogenation rates. To determine which step in this sequence is the rate-determining step, the sequential mechanism is analyzed using maximum rate analysis (described in Section S5 of the SI) to determine the kinetically relevant step by comparing the maximum rates of alkoxide formation and H_2 splitting. Protonated benzene and hexadiene cations are too stable and sterically hindered to form bound alkoxides, so these species were only investigated by the concerted hydrogenation mechanism. For formaldehyde, butadiene, and all alkenes studied here, alkoxide hydridation (eq 3) had maximum rates over 400× lower than alkoxide formation (eq 2) at all relevant conditions (553−723 K, 1−20 bar H_2, 0.01−0.15 bar reactant, Figure S5 of the SI), indicating that alkoxide formation from unsaturated compounds will be quasi-equilibrated within the timescale of hydrogenation reactions and therefore subsequent discussion will focus on alkoxide hydridation as it is the kinetically relevant step of the sequential mechanism in all zeolite frameworks investigated (Figures S4−S6).

The most facile concerted ethene hydrogenation transition state involves simultaneous protonation from O14 and heterolytic H_2 splitting to re-form a proton at O16 with the organic compound residing in the straight channel (Figure 3c), rather than the channel intersection. Exploring the effects of transition-state confinement is crucial to understanding the effects of topology on zeolite-catalyzed reactions, hence each of the reactions in this work was investigated at all possible O-site combinations within MFI and systematically reoriented as described in Section 2.2. Generally, aliphatic compounds, such as C_2H_4, reside in the straight channel of MFI as it is appropriately sized for small transition states, where dispersive interactions between the transition state and the framework are most favorable. This reaction occurs with an identical $\Delta G^{\ddagger}$ (220 kJ mol^{-1}) to that of ethoxide hydridation (Figure 3b), indicating that the concerted and sequential mechanisms compete at 623 K, while having slightly different $\Delta H^{\ddagger}$ (73 and 56 kJ mol^{-1} for alkoxide hydridation and concerted hydrogenation, respectively) indicates that other temperatures may lead to a single dominant mechanism. Concerted and sequential free-energy barriers are similar for all species as the transition states for both structures primarily involve a carbocation (fully or partially formed) interacting with a cleaving H_2 molecule, which is also interacting with the zeolite framework. Moreover, their rate equations reflect identical pressure dependences and, thus, these data yield identical predicted rates for each pathway in ethene hydrogenation at 623 K—making them indistinguishable by kinetic studies.

DFT-predicted kinetic isotope effects (KIEs) for the concerted and sequential mechanisms are 2.4 and 2.6, respectively, for 1-C_4D_8−D_2 reactions over D-MFI and 1.7 and 1.1 for C_2D_4−H_2 reactions over D-MFI. These are the only meaningful D-involving reactions as H/D on C_2H_4 and the zeolite surface will scramble in the quasi-equilibrated formation of alkoxides (or protonated complexes) from unsaturated compounds. These KIE values for 1-butene hydrogenation, furthermore, are not affected by the zeotype catalyst or by the reactant being considered, as shown in Table S3 of the SI. Ultimately, the predicted KIE values for the concerted and sequential mechanisms for completely or partially deuterated reactions are likely too close to one another to provide an effective experimental discrimination between these two reaction mechanisms.

The effective free-energy barriers for ethene hydrogenation are at least 40 kJ mol^{-1} higher than that for all other alkene species (Figure 4), because the short-lived primary carbenium ion ($C_2H_5^+$) is unstable relative to the secondary carbenium ions that can be formed from larger alkenes. Kinetic studies in H-SAPO-34 demonstrate that co-feeding H_2 can decrease the C_2H_4/C_3H_6 ratio by 1.3 times (16 bar H_2, 0.13 bar CH_3OH, 723 K),[37] which appears at odds with the DFT data presented in this work. However, it is unlikely that direct hydrogenation of ethene is the cause of this shift in ethene to propene ratios. Instead, H_2 limits the formation of aromatic species through elimination of CH_2O and dienes, thus limiting the rate of the aromatics-based cycle and influencing ethene to propene ratios.

There are two unique hydrogenation schemes for propene: formation of a primary carbocation by protonation of the secondary (β) carbon (Figure 5b) or formation of the secondary carbocation by protonation of the primary (α)

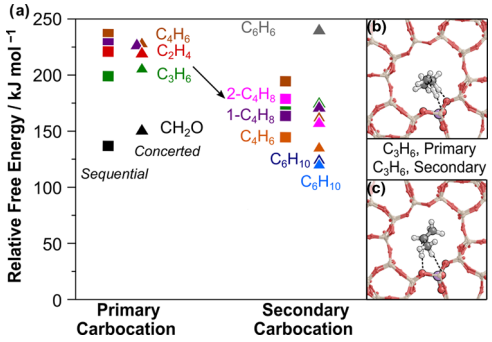

Figure 5. (a) Free energies of concerted (triangle) and sequential (square) hydrogenation transition states, and (b) primary and (c) secondary concerted C_3H_6 transition states.

https://dx.doi.org/10.1021/acscatal.9b04529
ACS Catal. 2020, 10, 4593−4607

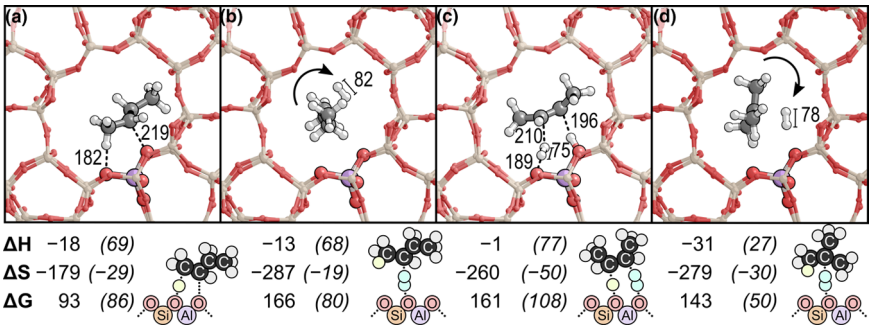

Figure 6. Most favorable transition-state structures of (a) forming a β-bound alkoxide from 1-butene, (b) hydridating a β-bound alkoxide from 1-butene, (c) concerted hydrogenation of 2-butene, and (d) hydridation of isobutene. Enthalpy (H, kJ mol^{-1}), entropy (S, J mol^{-1} K^{-1}) and free-energy (G, kJ mol^{-1}) barriers are reported at 623 K and 1 bar. Bond distances are reported in pm. Effective barriers (referenced to gas-phase species, $\Delta G^{\ddagger}$) and intrinsic barriers (in parentheses, ΔG_{act}) are both listed. Yellow- and blue-shaded H-atoms represent those from the zeolite and H_2, respectively.

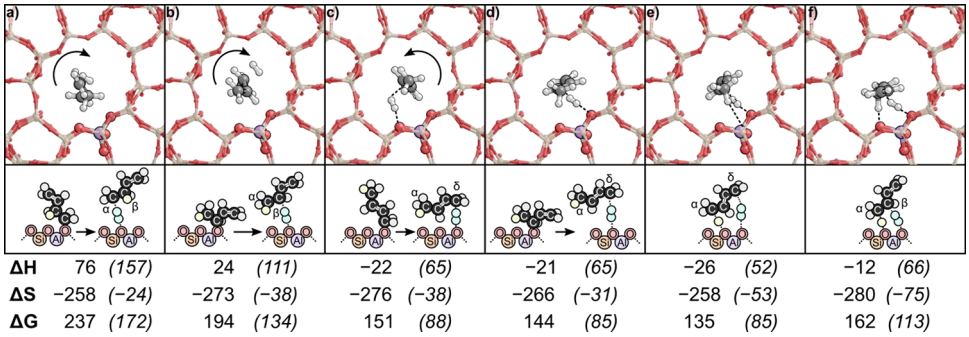

Figure 7. Most favorable transition-state structures of (a) hydridation of an α-bound surface intermediate to form 1-butene, (b) hydridation of a β-bound surface intermediate to form 1-butene, (c) δ-hydridation of an α-bound surface intermediate to form 2-butene, (d) δ-hydridation of a β-bound surface intermediate to form 2-butene, (e) concerted α,δ-hydrogenation of butadiene to 2-butene, (f) concerted α,β-hydrogenation of butadiene to 1-butene. Effective and intrinsic (italics, parentheses) free-energy barriers are reported in kJ mol^{-1} at 623 K. Yellow- and blue-shaded H-atoms represent those from the zeolite and H_2, respectively.

carbon (Figure 5c). Secondary carbocations are significantly more stable than primary carbocations, leading to lower hydrogenation barriers (Figure 5a) via those species. DFT calculations on 8T clusters of H-ZSM-5 demonstrate that barriers of dehydrogenation occurring on the β-carbon are 50−55 kJ mol^{-1} lower than dehydrogenation at the α-carbon,[72] further demonstrating the stability of secondary carbocations in these reactions. This trend is consistent across all species investigated (Figure 5a), indicating that carbocation stability is a good predictor of hydrogenation barriers among similar reactants (such as alkenes). The $\Delta G^{\ddagger}$ for propene hydrogenation via concerted and sequential hydrogenation (174 and 170 kJ mol^{-1}) are similar to one another, indicating that both mechanisms compete in MFI, and are lower than those of ethene (220 kJ mol^{-1}) as shown in Figure 4 because propene hydrogenation occurs via secondary carbenium ions. This is corroborated by experimental results that indicate small increases in C_3 alkane selectivity (16 bar H_2, 0.13 bar CH_3OH, 723 K)[37] and that the rate constants of ethene hydrogenation in H-SSZ-13 (CHA), H-SSZ-39 (AEI), H-FER, and H-BEA are 1.5−16× lower than the rate constants of propene hydrogenation.[39]

Concerted hydrogenation of 1-butene, like propene, also occurs by protonation of the primary α-C and hydridation of the secondary β-C (Figure 6c). Routes via secondary carbenium ions have $\Delta G^{\ddagger}$ that are >40 kJ mol^{-1} lower than routes proceeding via primary carbenium ions (Figure 5a). The effective free-energy barriers for hydrogenating 1-butene and 2-butene are nearly identical, 166 and 161 kJ mol^{-1} (Figure 4)—indicating that hydrogenation is equally as likely to occur regardless of the n-butene isomer present in the hydrocarbon pool. n-Butene hydrogenation barriers are significantly lower than those of ethene, but within 9 kJ mol^{-1} of propene, suggesting that alkylcarbenium stability plays a larger role than the carbon-chain length in alkyl hydrogenation rates. This is confirmed by analysis of isobutene hydrogenation, which most favorably occurs via hydridation of a surface-bound $C(CH_3)_3$−Z species. The transition state is 18 kJ mol^{-1} more stable than n-butene hydrogenation transition states, confirming that branched alkenes, such as isobutene, are most readily hydrogenated, followed by n-alkenes ($n > 2$), and then ethene, following carbenium stabilities 1° < 2° < 3°.

Dienes can react with aromatics to form large polyaromatic species that deactivate zeolite catalysts; therefore, elimination of butadiene species through hydrogenation is one possible mechanism through which H_2 co-feeds elongate catalyst lifetime. The measured second-order rate constants of butadiene hydrogenation in H-CHA (H-SSZ-13), H-SSZ-39, H-FER, and H-BEA are 7−300× larger than the rate constants of ethene and propene hydrogenation, suggesting that butadiene is selectively hydrogenated regardless of zeolite topology.[39] This selective butadiene hydrogenation, however, is not because of a thermodynamic preference as reaction free energies for diene hydrogenation (−33 to −50 kJ mol^{-1}) are similar to those of alkene hydrogenation (−33 to −63 kJ mol^{-1}) (Figure 2). Butadiene can be hydrogenated to form 1-

https://dx.doi.org/10.1021/acscatal.9b04529
ACS Catal. 2020, 10, 4593−4607

butene (via α,β attack) and 2-butene (via α,δ attack), leading to four unique alkoxide-hydridation reactions (eq 3 and Figure 7a–d) and two unique concerted hydrogenation routes (eq 1 and Figure 7e,f). The alkoxide-hydridation transition states (sequential mechanism) depicted in Figure 7a–c involve formation of a carbenium followed by rotation to reach the orientation in which hydridation can occur. As such, the transition state for these species involves both rotation and H_2 stretching. The transition state shown in Figure 7d represents alkoxide hydridation; however, unlike Figure 7a–c, this route does not require rotation of $C_4H_7^+$ because the δ-carbon is being hydridated (rather than the surface-bound carbon), and occurs with the lowest sequential barrier (by >7 kJ mol^{-1}) of 144 kJ mol^{-1} (Figure 8). Alkoxide-hydridation transition-state

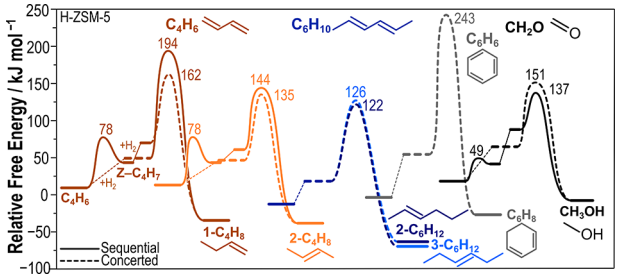

Figure 8. Reaction coordinate diagram of butadiene hydrogenation to 1-butene (brown) and 2-butene (orange), hexadiene hydrogenation to 2-hexene (dark blue) and 3-hexene (light blue), benzene (gray), and formaldehyde (black) via concerted (dashed) and sequential (solid) mechanisms in H-ZSM-5. Free energies (kJ mol^{-1}) are reported at 623 K. All enthalpy, entropy, and free-energy barriers are reported in Table S6 and transition-state structures are shown in Section S8.

barriers (Figure 7a–d) tend to reflect both the stability of carbenium formed and the position of hydrogenation. Barriers among sequential hydrogenation transition states with secondary allylic carbeniums (Figure 7b–d) are between 144 and 194 kJ mol^{-1} (Figure 8) and are 40 kJ mol^{-1} lower in $\Delta G^{\ddagger}$ than the reaction via a non-allylic primary carbenium cation (Figure 7a). Furthermore, allylic carbocations result in transition states ~10 kJ mol^{-1} lower than secondary alkylcarbenium transition states (161–166 kJ mol^{-1}, Figure 4) for butene hydrogenation. Additionally, α,δ-hydrogenation transition states (Figure 7c,d) are >30 kJ mol^{-1} more stable than α,β transition states (Figure 7a,b) in the sequential mechanism. Similarly, α,δ schemes of concerted protonation and hydridation to form 2-butene are favored over α,β-hydrogenation—occurring with a $\Delta G^{\ddagger}$ 28 kJ mol^{-1} lower despite both reactions forming a secondary, allylic carbocation. Butadiene hydrogenation occurs with barriers up to 20 kJ mol^{-1} lower than those of butene; however, this preference is not fully explained by increased carbocation stabilities as butadiene shows a unique preference of α,δ-hydrogenation schemes. Furthermore, barriers of α,β-hydrogenation of butadiene ($\Delta G^{\ddagger}$ of 162 kJ mol^{-1}, Figure 8) are essentially identical to propene and butene hydrogenation barriers ($\Delta G^{\ddagger}$ of 161 kJ mol^{-1}, Figure 4), while α,δ-hydrogenation of butadiene occurs with a barrier of 135 kJ mol^{-1}. The preference to form 2-butene from butadiene cannot be experimentally verified as double bond and skeletal isomerization are facile, resulting in an equilibrated mixture of isobutene, 1-butene, and 2-butene at MTO and hydrogenation conditions. This inability of the experiments to determine the primary butadiene hydrogenation product further motivates our theoretical studies. Overall, formation of allylic carbocations results in energy barriers lower than those of alkylcarbeniums, further demonstrating that hydrogenation barriers are governed by carbocation stabilities and the availability of α,δ-hydrogenation schemes, which, we hypothesize, reduce steric hindrances associated with hydridation.

Hexadiene can hydrogenate to form 2-hexene via α,β-attack (Figures 9a) or 3-hexene via α,δ-attack (Figure 9b). Protonated hexadiene is relatively stable (ΔG of 8 kJ mol^{-1}, Table S5) because it forms an allylic carbocation and the C_6 chain offers increased charged distribution compared to C_2–C_4 chains; in contrast, C_2–C_4 carbenium ions are unstable (>100 kJ mol^{-1} relative to gas, Table S5) when protonated. The stability of the hexadiene carbocation alters the nature of the concerted transition state compared to those of C_2–C_4 alkenes. Protonation is nearly complete prior to hydridation; therefore, the transition state only involves heterolytic cleavage of H_2 (Figure 9a,b) rather than simultaneous protonation and hydridation as seen in C_2–C_4 compounds. As such, we predict that concerted and sequential hydrogenation transition states will be nearly identical in both structure and energy, similar to the trends observed for butadiene. Moreover, the C_6H_{11}–Z species is unstable compared to the protonated state (ΔG of 46 kJ mol^{-1} relative to gas-phase species, Table S5). Combining the instability of C_6H_{11}–Z and the likely small energy differences between concerted and sequential hydrogenation, we have only investigated the concerted mechanism of hexadiene hydrogenation. Hexadiene does not demonstrate a strong preference towards either α,β ($\Delta G^{\ddagger}$ of 122 kJ mol^{-1} to

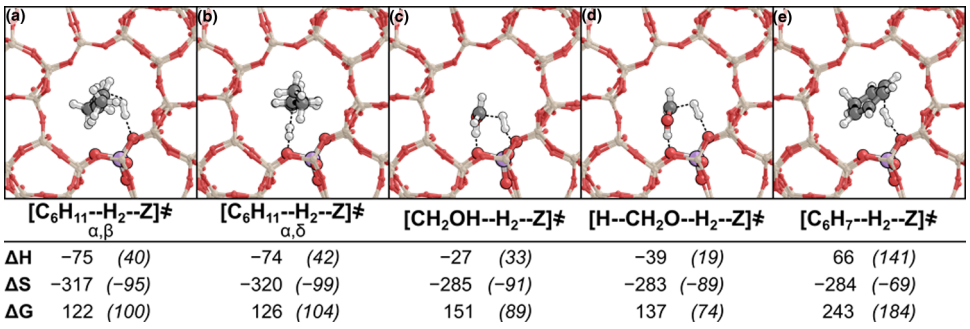

Figure 9. Most favorable transition states of hexadiene hydrogenation to (a) 2-hexene and (b) 3-hexene, (c) CH_2OH–Z hydridation, (d) concerted CH_2O hydrogenation, and (e) benzene hydridation. Effective and intrinsic (italics, parentheses) enthalpies (kJ mol^{-1}), entropies (J K^{-1} mol^{-1}), and free energies (kJ mol^{-1}) are reported at 623 K.

https://dx.doi.org/10.1021/acscatal.9b04529
ACS Catal. 2020, 10, 4593–4607

2-hexene) or α,δ ($\Delta G^{\ddagger}$ 126 kJ mol^{-1} to 3-hexene) hydrogenation schemes. The barriers of hexadiene hydrogenation are >10 kJ mol^{-1} lower than those of butadiene, indicating that the longer chain length lowers hydrogenation barriers because of increased charge distribution across the carbon chain.

Previous literature has implicated CH_2O as a precursor to dienes and aromatics and as a significant contributor to catalyst deactivation.[26,47,48,73,74] Kinetic studies have demonstrated that co-feeding H_2 and CH_2O (4 bar H_2, 0.13 mbar CH_2O, 0.13 bar CH_3OH, 673 K) increases catalyst lifetimes by 2.1-fold compared to identical co-feeds of He and CH_2O. This indicates that H_2 may limit polyaromatic formation by intercepting CH_2O diene precursors. Therefore, we investigated CH_2O hydrogenation in MFI and compared it to diene hydrogenation reactions to determine if deactivation is limited by direct hydrogenation of dienic species (i.e., arene precursors) or hydrogenation of diene precursors to prevent the initial formation of dienes. Concerted CH_2O hydrogenation to form oxocarbeniums (CH_2OH^+, Figure 9d) via O-protonation is >100 kJ mol^{-1} more favorable than C-protonation to form CH_3O^+. Similarly, the sequential mechanism involves formation and hydridation of a hydroxyalkoxide (HOH_2C-Z) (Figure 9c). Hydrogenation of CH_2O occurs with $\Delta G^{\ddagger}$ of 144 kJ mol^{-1}, which is consistent with previous studies suggesting that barriers of CH_2O hydrogenation are lower than those of ethene hydrogenation.[42] Despite the shorter chain length, these hydrogenation barriers are within 10 kJ mol^{-1} of butadiene ($\Delta G^{\ddagger}$ of 135 kJ mol^{-1}) likely because of the relative stability of oxocarbenium ions (Figure 2) coupled with hydrogen bonding between the framework and −OH of the transition state. This suggests that aromatic and polyaromatic formation during MTO is limited by both direct diene hydrogenation and hydrogenation of CH_2O, which is a diene precursor species. Moreover, this further supports that H_2 co-feeds alter C_2H_4/C_3H_6 ratios by preventing the formation of aromatic species—through elimination of dienes and diene precursors—and thus the aromatic-based cycle is indirectly limited, as suggested in previous work.[37]

The benzene hydrogenation transition state involves only heterolytic cleavage of H_2 as protonated benzenium cations are relatively stable compared to aliphatic carbenium ions. Moreover, $C_6H_7^+$ (ΔG of 96 kJ mol^{-1} relative to gas-phase species, Table S5) is significantly more stable than C_6H_7-Z species (ΔG of 341 kJ mol^{-1} relative to gas-phase species, Table S5); therefore, alkoxide-formation and alkoxide-hydridation pathways were not considered for benzene. Free-energy barriers associated with benzene hydridation (243 kJ mol^{-1}, Figure 8) are significantly higher than all investigated alkenes and dienes, because breaking the aromaticity of the benzene ring results in unstable states. This is consistent with previous experimental studies suggesting that benzene does not react with hydrogen unless there are tertiary hydride sources present.[40] Benzene hydrogenation routes are insignificant at high H_2 MTO conditions, so direct arene hydrogenation does not contribute to decreases in deactivation rates in MFI.[37,38] Rather, the formation of polyaromatics is limited through elimination of CH_2O and dienes.

3.3. Hydrogenation in H-CHA (H-SSZ-13). Concerted and sequential hydrogenation reactions were also investigated in the CHA framework, which is topologically distinct from MFI. MFI contains straight and sinusoidal channels that intersect to form the channel intersection, where T11 is situated, and the three accessible O-sites of T11 reside in the straight channel (O14) or bridge the straight channel and channel intersection (O16 and O25). This work, and previous work,[66] have demonstrated that the straight channel of H-ZSM-5 offers confinement for smaller transition states, such as those associated with the hydrogenation of small molecules like those investigated here. Conversely, the O-sites of H-SSZ-13 (CHA) each have different chemical environments: O1 bridges a six-membered-ring (6-MR) and two four-MRs, O2 spans two eight-MRs, O3 spans the six-MR and eight-MR, and O4 spans the eight-MR and four-MR (Figure S2). Similar to MFI, hydrogenation of C_2-C_4 alkenes, C_4 and C_6 dienes, benzene, and CH_2O was investigated at all O-site combinations within H-SSZ-13.

Alkene hydrogenation in H-SSZ-13 (Figure 10) occurs with similar trends as observed in MFI. Maximum rate analysis is used to identify the rate-determining step of the sequential mechanism and rates of alkoxide hydridation are >400× lower (553−723 K, 1−20 bar H_2, 0.01−0.15 bar reactant, Figure S6 of the SI) than rates of alkoxide formation; therefore, alkoxide hydridation is kinetically relevant (as observed for MFI) and the remainder of this discussion will focus on comparing alkoxide hydridation (of the sequential mechanism) and the concerted mechanism. There are two distinct alkoxide hydridation transition states: heterolytic H_2 cleavage (Figure 11b,d,e bottom) and alkoxide rotation (Figure 11a,c, bottom). The instability of primary carbocations causes an earlier transition state that includes rotation, whereas transition states of secondary and tertiary carbocations primarily involve heterolytic cleavage of H_2. Previous work has shown that H-SSZ-13 and H-ZSM-5 have similar predicted acid strengths (as measured by the deprotonation energy);[75] however, alkene hydrogenation barriers in H-SSZ-13 (Figure 10) are on average 10 kJ mol^{-1} lower than those in H-ZSM-5 (Figure 4). One possible explanation for the lower barriers is that the topology of H-SSZ-13 offers additional stabilization to alkylcarbenium transition states as compared to H-ZSM-5.

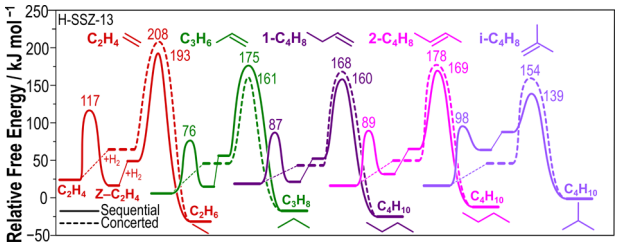

Figure 10. Free-energy barriers of ethene (red), propene (green), 1-butene (dark purple), 2-butene (pink), and isobutene (light purple) via concerted (dashed) and sequential (solid) mechanisms in H-SSZ-13. Free energies (kJ mol^{-1}) are reported at 623 K and 1 bar of each species (alkene and H_2). All enthalpy, entropy, and free-energy barriers are reported in Table S6 and transition-state structures are shown in Section S8.

Barriers of butadiene hydrogenation (150 and 152 kJ mol^{-1}, Figure 12) are lower than those of primary and secondary alkene hydrogenation (161−193 kJ mol^{-1}, Figure 10); however, isobutene hydrogenation (139 kJ mol^{-1}) occurs with a barrier 11 kJ mol^{-1} lower than that of butadiene. Butadiene hydrogenation is preferred over linear alkenes and will contribute to the elimination of deactivating species. DFT-predicted rate constants suggest that rates of butadiene

https://dx.doi.org/10.1021/acscatal.9b04529
ACS Catal. 2020, 10, 4593−4607

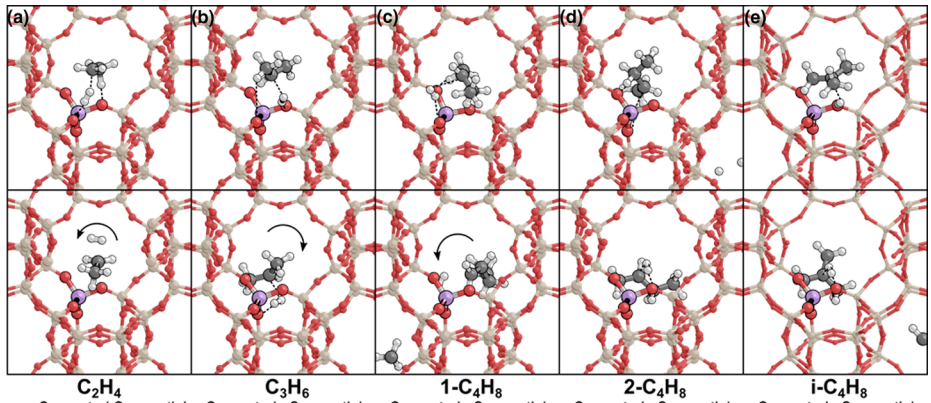

	C_2H_4		C_3H_6		1-C_4H_8		2-C_4H_8		i-C_4H_8	
	Concerted	Sequential	Concerted	Sequential	Concerted	Sequential	Concerted	Sequential	Concerted	Sequential
ΔH	31	18	3	2	−16	−21	4	−5	−18	−41
ΔS	−284	−281	−254	−278	−294	−290	−280	−280	−277	−288
ΔG	208	193	161	175	168	160	178	169	154	139

Figure 11. Most favorable concerted (top) and sequential (bottom) transition states of (a) ethene, (b) propene, (c) 1-butene, (d) 2-butene, and (e) isobutene. Enthalpies (kJ mol^{-1}), entropies (J K^{-1} mol^{-1}), and free energies (kJ mol^{-1}) are reported relative to the gas-phase energies at 623 K.

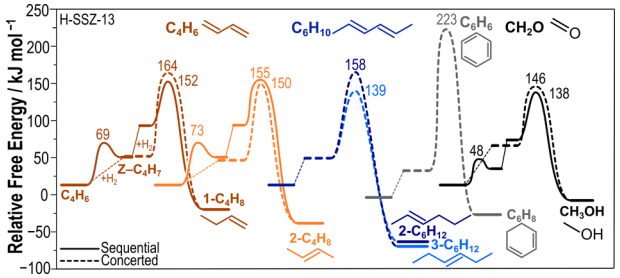

Figure 12. Reaction coordinate diagram of butadiene hydrogenation to 1-butene (brown) and 2-butene (orange), hexadiene hydrogenation to 2-hexene (dark blue) and 3-hexene (light blue), benzene (gray), and formaldehyde (black) via concerted (dashed) and sequential (solid) mechanisms in H-SSZ-13. Free energies (kJ mol^{-1}) are reported at 623 K. All enthalpy, entropy, and free-energy barriers are reported in Table S7 and transition-state structures are shown in Section S8.

hydrogenation are ∼76× those of propene hydrogenation and 1000× higher than those of ethene hydrogenation (Figure S6). Kinetic studies co-feeding 1,3-butadiene (H-SSZ-13, 1−16 bar H_2, 0.1−1 mbar C_2H_4 or C_3H_6 or C_4H_6, 673 K) predict that butadiene hydrogenation rates are 185-fold higher than those of propene hydrogenation and 263-fold higher than those of ethene hydrogenation in H-SSZ-13,[39] indicating that the relative rates as predicted by DFT are within factors of 3 of the measured relative rates. Unlike MFI, barriers to form 2-butene are not significantly favored over 1-butene formation (4 kJ mol^{-1} in H-SSZ-13 compared to 19 kJ mol^{-1} in H-ZSM-5), suggesting that the α,δ versus α,β hydrogenation schemes do not play a significant role in determining hydrogenation product selectivity in H-SSZ-13. As such, it is likely that H-SSZ-13 forms a mixture of butene isomers during the hydrogenation process.

Similar to MFI, hexadiene hydrogenation barriers are lower than those of butadiene barriers, because longer C-chains facilitate charge distribution. Unlike H-ZSM-5, H-SSZ-13 demonstrates a stronger preference to form 3-hexene via α,δ-hydrogenation of hexadiene (by 17 kJ mol^{-1}) over α,β-hydrogenation to form 2-hexene—likely caused by differences in local topologies between the two frameworks shifting product selectivity. Benzene hydrogenation remains unfavorable in the H-SSZ-13 framework, further supporting that H_2 does not directly eliminate aromatic species. Barriers for CH_2O hydrogenation ($\Delta G^{\ddagger}$ of 138 and 146 kJ mol^{-1}, Figure 12) are lower than those of alkene hydrogenation ($\Delta G^{\ddagger}$ of 160−193 kJ mol^{-1}), consistent with previous DFT-predictions.[42] Furthermore, CH_2O hydrogenation barriers are lower than those of butadiene hydrogenation ($\Delta G^{\ddagger}$ of 150 kJ mol^{-1}), indicating CH_2O elimination may play a more critical role in H-SSZ-13 frameworks as compared to H-ZSM-5 frameworks. Therefore, deactivation in H-SSZ-13 is likely prevented through both direct hydrogenation of dienes and hydrogenation of CH_2O to prevent diene formation, rather than elimination of aromatic species.

3.4. Hydrogenation in H-SAPO-34 (CHA Framework).

High pressure H_2 co-feeds have been shown to increase catalyst lifetimes in H-SAPO-34 by a factor of 10 (673 K, 4 bar H_2, 0.13 bar CH_3OH), demonstrating that high H_2 co-feeds can increase catalyst lifetimes in a variety of different zeolite framework topologies. Here, we will compare the trends in transition-state energy barriers in H-SSZ-13 and H-SAPO-34 to determine the effects of acid strength on hydrogenation pathways.

The trends in sequential and concerted hydrogenation are similar to those observed in H-ZSM-5 (Section 3.2) and H-SSZ-13 (Section 3.3); therefore, this discussion will focus

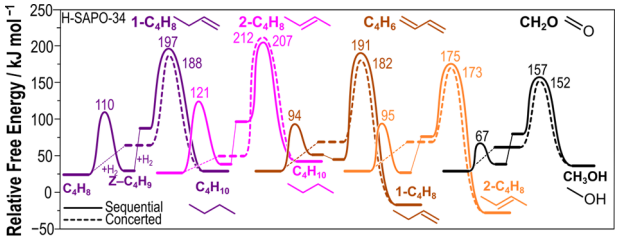

Figure 13. Reaction coordinate diagram of 1-butene (orange) and 2-butene (gray) hydrogenation to butadiene, butadiene hydrogenation to 1-butene (yellow) and 2-butene (blue), hexadiene hydrogenation to 2-hexene (green) and 3-hexene (dark blue) and formaldehyde (blue) via concerted mechanisms. Free energies (kJ mol^{-1}) are reported at 623 K. All enthalpy, entropy, and free-energy barriers are reported in Table S8 and transition-state structures are shown in Section S8.

https://dx.doi.org/10.1021/acscatal.9b04529
ACS Catal. 2020, 10, 4593−4607

primarily on hydrogenation of butene, dienes, and CH_2O. The α,δ-attack mechanism of butadiene is 9 kJ mol^{-1} more favorable than comparable α,β-attack mechanisms (Figure 13). Additionally, isobutene hydrogenation is 12 kJ mol^{-1} more favorable than *n*-butene and comparable to those of butadiene (3 kJ mol^{-1} difference). Notably, unlike H-SSZ-13 and H-ZSM-5, CH_2O hydrogenation barriers are significantly lower than those of butadiene and hexadiene. This increased favorability toward CH_2O hydrogenation in H-SAPO-34 is likely because Al−O bonds are more polar than Si−O bonds, lending to increased hydrogen bonding between the CH_2O transition state and zeolite framework. This suggests that deactivation in H-SAPO-34 is primarily limited by hydrogenation of CH_2O, or diene precursors, to prevent formation of dienic compounds, rather than elimination of both dienes and diene precursors as observed in H-ZSM-5 and H-SSZ-13.

3.5. Comparing H-SAPO-34, H-SSZ-13, and H-ZSM-5. Generally, trends among the aluminosilicate frameworks (H-ZSM-5 and H-SSZ-13) and phosphoaluminosilicate framework (H-SAPO-34) are similar (Figure 14). Hydrogenation barriers

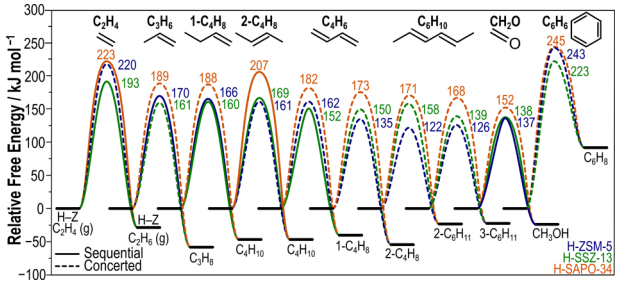

Figure 14. Hydrogenation energies relative to gas-phase species in H-ZSM-5 (MFI, blue), H-SSZ-13 (CHA, green), and H-SAPO-34 (CHA, orange). Figure S8 of the SI shows the same data generated using the BEEF-vdW functional.

decrease as the length of the carbon-chain increases for both alkenes and dienes in all three zeotype catalysts. Butadiene hydrogenation is facilitated by forming an allylic carbocation (Figure 14) and preferentially forms 2-butene instead of 1-butene in H-ZSM-5 and H-SAPO-34—indicating that the α,δ hydrogenation scheme may play a role in its relatively low barriers. Formaldehyde hydrogenates with similar barriers to butadiene, as described below, and benzene hydrogenates with barriers significantly larger than those for all other species.

Comparing the two aluminosilicates (H-SSZ-13 and H-ZSM-5), hydrogenation free-energy barriers (relative to gas-phase species) are generally similar (most are within 12 kJ mol^{-1} of one another), with H-SSZ-13 having slightly lower barriers, on average, than H-ZSM-5. Effective free-energy barriers for hydrogenation reactions in H-SAPO-34 are 12−38 kJ mol^{-1} higher than those in H-SSZ-13 (Figure 15)—indicating that the decreased acid strength of H-SAPO-34 results in lower hydrogenation rates and that this effect is approximately even across the hydrocarbon molecules and mechanisms studied here. C_6H_{10} and CH_2O hydrogenation barriers are just 12 and 14 kJ mol^{-1} higher, respectively, the least destabilized by the decreased acid strength, likely because these species hydrogenate through relatively stable carbocations compared to others. Notably, barriers in H-SAPO-34 are consistently higher than those in H-ZSM-5 and H-SSZ-13; however, kinetic studies demonstrate that H_2 co-feeds prolong catalyst lifetimes most effectively in H-SAPO-34.[37] There are many competing reaction pathways in the MTO network, including hydrogenation, product formation, and deactivation. To make conclusions regarding the efficiency of catalyst lifetime improvement, a comprehensive investigation of these main reaction networks is required. However, higher barriers in H-SSZ-13 are consistent with predicted scaling relationships, suggesting that weaker acid sites are less reactive during MTO chemistry.[76,77] Additionally, previous studies comparing rates of MTO initiation (PBE-D3)[78] and alkene formation routes (BEEF-vdw)[79] in H-SSZ-13 and H-SAPO-34 indicate that barriers in H-SAPO-34 are ∼15−30 kJ mol^{-1} higher than those in H-SSZ-13—indicating that higher hydrogenation barriers are likely also coupled with higher product-formation barriers in H-SAPO-34. A complete study of the MTO cycle is outside of the scope of this work, which demonstrates that the extension of catalyst lifetimes is caused by hydrogenation of dienes and diene precursor species (formaldehyde).

Formaldehyde hydrogenates with barriers 2 kJ mol^{-1} higher than in butadiene in H-ZSM-5 and with barriers 12 and 21 kJ mol^{-1} lower than in butadiene in H-SSZ-13 and H-SAPO-34, respectively. As such, hydrogenation of diene precursors (CH_2O) may also play a key role in increasing catalyst lifetimes, perhaps more so in CHA frameworks. Prior reports,[62] however, have indicated that formaldehyde hydrogenation barriers are underestimated with PBE-D3 compared to the CCSD methods applied to cluster models, and that the BEEF-vdW functional gives better agreement with those of CCSD methods. Trends between zeolite frameworks and hydrogenation barriers remain consistent in our BEEF-vdW calculations (Figure S8). BEEF-vdW free energies of hydrocarbon hydrogenation tend to be within ∼10 kJ mol^{-1} of PBE-D3-obtained free energies, with a few exceptions. Generally, the conclusions one would reach using the BEEF-vdW functional would be the same as those reached here, that H_2 extends catalyst lifetimes through a combination of diene and formaldehyde hydrogenation, with the relative rates of those pathways being dictated by the relative concentrations of those species in the zeolite during MTO reactions, which itself depends on many factors.

3.6. Effects of H_2O. The effects of H_2O on hydrogenation barriers were investigated as recent studies have demonstrated that co-feeding high pressures of H_2 and H_2O further increases catalyst lifetimes from 75 h (4.2 bar CH_3OH, 35.7 bar H_2, 723 K) to 118 h (4.2 bar CH_3OH, 22.8 bar H_2, 12.8 bar H_2O, 723 K) as measured by the time at which methanol conversion dips beneath 80%.[38] Concerted hydrogenation of 2-butene, butadiene, and CH_2O was modeled with H_2O in all three zeolite catalysts (Figure 15a−c) to determine if H_2O facilitates hydrogenation reactions by facilitating protonation and lowering free-energy barriers. The transition state is remarkably similar in all three frameworks and involves H_2O facilitating proton transfer and stabilizing the carbocation with simultaneous hydridation of the guest species by H_2. The increased hydrogen bonding in the transition state lowers effective enthalpy barriers ($\Delta H^{\ddagger}$) by 34−97 kJ mol^{-1} compared to routes without H_2O. This indicates that H_2O can enthalpically stabilize these transition-state formations by interacting with the carbocation and conjugate base of the acid site; however, it does so by sacrificing significant entropy compared to gas-phase H_2O. The entropic losses outweigh the enthalpic gains in the free energies as all transition states facilitated by H_2O occur with $\Delta G^{\ddagger}$ of 5−40 kJ mol^{-1} higher than transition states with just H_2 (Figure 15d). This indicates that H_2O does not

https://dx.doi.org/10.1021/acscatal.9b04529
ACS Catal. 2020, 10, 4593−4607

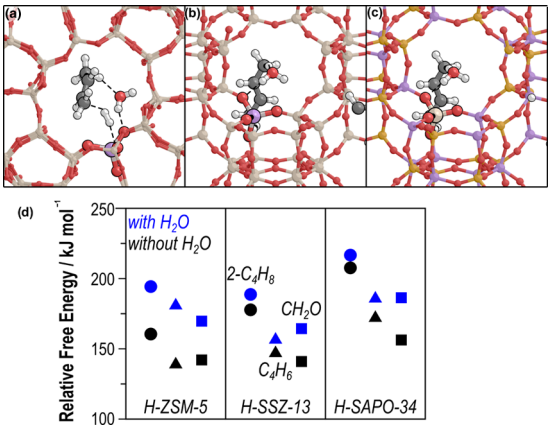

Figure 15. Images of H_2O-assisted concerted butadiene transition state in (a) H-ZSM-5 (MFI), (b) H-SSZ-13 (CHA), and (c) H-SAPO-34 (CHA) and (d) shows concerted relative free energies for 2-butene (●), butadiene (■), and formaldehyde (▲) hydrogenation with H_2O (blue) and without H_2O (black). Free energies are reported at 623 K and 1 bar for all reactants. Entropy and enthalpy barriers are tabulated in Table S9 of the SI.

directly facilitate hydrogenation reactions except at very high H_2O/H_2 ratios; rather, increased lifetimes with H_2O pressures are likely caused by an increase in the number of available protons through either competitive adsorption of H_2O with CH_3OH at acid sites to prevent formation of CH_3−Z species or CH_3−Z + H_2O → H−Z + CH_3OH reactions, which remove surface methyl species. If surface methylation is rapid and quasi-equilibrated, then the concentration of methyl species is inversely proportional to H_2O pressure, and thus proton coverages and therefore hydrogenation rates increase with H_2O pressure, as observed.

4. CONCLUSIONS

Here, we investigate concerted and sequential diene hydrogenation schemes for C_2−C_4 alkenes, C_4 and C_6 dienes, benzene, and CH_2O to determine the mechanism by which high pressure H_2 co-feeds improve catalyst lifetime. DFT-predicted and rates for sequential and concerted hydrogenation are within the errors of DFT methods in all cases, indicating that the two hydrogenation mechanisms compete during catalysis and cannot be distinguished using theory or isotopic studies. For both mechanisms, the limiting portion of the reaction is the heterolytic H_2 dissociation that transfers a hydride to a carbocation. Generally, hydrogenation barriers in the two aluminosilicate frameworks H-SSZ-13 and H-ZSM-5 (CHA and MFI) are within 15 kJ mol^{-1} of one another and hydrogenation barriers follow nearly identical trends between the two frameworks, despite the different confining void topologies. Additionally, interchanging the aluminosilicate CHA framework (H-SSZ-13) with phosphoaluminosilicate CHA framework (H-SAPO-34) results in systematic increases of hydrogenation barriers by an average of 26 kJ mol^{-1} because of the weaker acid strength in H-SAPO-34.

Alkene hydrogenation proceeds via the formation of secondary and tertiary alkylcarbenium ions, when possible, over primary carbenium ions, which are less stable (by 20−70 kJ mol^{-1}), resulting in lower hydrogenation barriers for C_3 and C_4 alkenes compared to C_2. The oxocarbenium ions formed in CH_2O hydrogenation are stable and result in low hydrogenation barriers. Benzenium carbocations cannot overcome the thermodynamic instability of benzene hydrogenation, resulting in large barriers associated with benzene hydrogenation. Allylic carbocations are formed during diene hydrogenations and are more stable than primary and secondary alkylcarbenium cations (formed in alkene hydrogenations), and hydrogenation of dienes is further accelerated by increasing the carbon-chain length as hydrogenation barriers of hexadiene are 10−20 kJ mol^{-1} lower than those of butadiene.

The main mechanism of lifetime improvement is by limiting the formation of deactivation precursors—dienes and CH_2O. Direct hydrogenation barriers of butadiene are relatively low (135 kJ mol^{-1} in ZSM-5, 150 kJ mol^{-1} in SSZ-13, and 173 kJ mol^{-1} in SAPO-34), as are those of hydrogenation of CH_2O, which plays a role in diene formation[26,47] (137 kJ mol^{-1} in ZSM-5, 138 kJ mol^{-1} in SSZ-13, and 152 kJ mol^{-1} in SAPO-34), with similar trends found for the PBE-D3 and BEEF-vdW functionals. The limited hydrogenation of alkenes combined with increases in catalyst lifetimes in MTO studies suggests that deactivation precursors must be selectively hydrogenated (i.e., hydrogenated at a higher rate) than the desired alkene products, and this is proven here as diene and formaldehyde hydrogenation occurs with barriers 9−37 kJ mol^{-1} lower than those for propene or butene hydrogenation and 43−85 kJ mol^{-1} lower than those for ethene hydrogenation. This indicates that dienes and CH_2O are selectively hydrogenated over alkenes, consistent with previous kinetic studies, suggesting that rate constants of butadiene hydrogenation are higher than those of C_2 and C_3 alkene hydrogenation.[39] Overall, hydrogenation of dienes and CH_2O is relatively facile compared to alkenes in MFI and CHA zeolite frameworks, demonstrating that diene prevention and elimination is the primary mechanism of catalyst lifetime improvement with high-pressure H_2 co-feeds.

■ ASSOCIATED CONTENT

Supporting Information

The Supporting Information is available free of charge at https://pubs.acs.org/doi/10.1021/acscatal.9b04529.

Structures of reactant product and transition states, detailed analysis of hydrogenation rates, formulas and details of frequency calculations for enthalpy and free-energy approximations, kinetic isotope effects, and all activation and reaction enthalpies and entropies (PDF)

All reactant, product, and transition state structure and reaction mode files (ZIP)

■ AUTHOR INFORMATION

Corresponding Author

David Hibbitts − *Department of Chemical Engineering, University of Florida, Gainesville, Florida 32611, United States*; orcid.org/0000-0001-8606-7000; Email: hibbitts@che.ufl.edu

Authors

Mykela DeLuca − *Department of Chemical Engineering, University of Florida, Gainesville, Florida 32611, United States*

Christina Janes − *Department of Chemical Engineering, University of Florida, Gainesville, Florida 32611, United States*

Complete contact information is available at: https://pubs.acs.org/10.1021/acscatal.9b04529

https://dx.doi.org/10.1021/acscatal.9b04529
ACS Catal. 2020, 10, 4593−4607

Notes

The authors declare no competing financial interest.

■ ACKNOWLEDGMENTS

This work was funded by an ACS Petroleum Research Fund New Doctoral Investigation Award (57079-DNI5). Partial support was provided by the NSF REU site grant (1852111) and the Summer Undergraduate Research at Florida (SURF) program. Computational resources were provided by the Extreme Science and Engineering Discovery Environment (XSEDE),[80] which is supported by the National Science Foundation grant number ACI-1548562 through allocation CTS160041. Additional computational resources were provided by the University of Florida Research Computing. The authors acknowledge Alexander Hoffman (University of Florida) and Abdulrahman Almithn (University of Florida) for thoughtful discussion and proofreading.

■ REFERENCES

(1) Ilias, S.; Bhan, A. Mechanism of the Catalytic Conversion of Methanol to Hydrocarbons. *ACS Catal.* **2013**, *3*, 18−31.
(2) Haw, J. F.; Song, W.; Marcus, D. M.; Nicholas, J. B. The Mechanism of Methanol to Hydrocarbon Catalysis. *Acc. Chem. Res.* **2003**, *36*, 317−326.
(3) Avidan, A. A. Gasoline and Distillate Fuels from Methanol. In *Studies in Surface Science and Catalysis*; Methane Conversion, Proceedings of a Symposium on the Production of Fuels and Chemicals from Natural Gas; Elsevier, 1988; Vol. *36*, pp 307−323.
(4) Blaszkowski, S. R.; van Santen, R. A. Theoretical Study of C−C Bond Formation in the Methanol-to-Gasoline Process. *J. Am. Chem. Soc.* **1997**, *119*, 5020−5027.
(5) Chang, C. D.; Kuo, J. C. W.; Lang, W. H.; Jacob, S. M.; Wise, J. J.; Silvestri, A. J. Process Studies on the Conversion of Methanol to Gasoline. *Ind. Eng. Chem. Proc. Des. Dev.* **1978**, *17*, 255−260.
(6) Johansson, R.; Hruby, S. L.; Rass-Hansen, J.; Christensen, C. H. The Hydrocarbon Pool in Ethanol-to-Gasoline over HZSM-5 Catalysts. *Catal. Lett.* **2009**, *127*, 1−6.
(7) Olsbye, U.; Svelle, S.; Lillerud, K. P.; Wei, Z. H.; Chen, Y. Y.; Li, J. F.; Wang, J. G.; Fan, W. B. The Formation and Degradation of Active Species During Methanol Conversion over Protonated Zeotype Catalysts. *Chem. Soc. Rev.* **2015**, *44*, 7155−7176.
(8) Hwang, A.; Bhan, A. Deactivation of Zeolites and Zeotypes in Methanol-to-Hydrocarbons Catalysis: Mechanisms and Circumvention. *Acc. Chem. Res.* **2019**, *52*, 2647−2656.
(9) Rojo-Gama, D.; Signorile, M.; Bonino, F.; Bordiga, S.; Olsbye, U.; Lillerud, K. P.; Beato, P.; Svelle, S. Structure−deactivation Relationships in Zeolites During the Methanol−to-hydrocarbons Reaction: Complementary Assessments of the Coke Content. *J. Catal.* **2017**, *351*, 33−48.
(10) Rojo-Gama, D.; Nielsen, M.; Wragg, D. S.; Dyballa, M.; Holzinger, J.; Falsig, H.; Lundegaard, L. F.; Beato, P.; Brogaard, R. Y.; Lillerud, K. P.; Olsbye, U.; Svelle, S. A Straightforward Descriptor for the Deactivation of Zeolite Catalyst H-ZSM-5. *ACS Catal.* **2017**, *7*, 8235−8246.
(11) Li, J.; Wei, Y.; Qi, Y.; Tian, P.; Li, B.; He, Y.; Chang, F.; Sun, X.; Liu, Z. Conversion of Methanol over H-ZSM-22: The Reaction Mechanism and Deactivation. *Catal. Today* **2011**, *164*, 288−292.
(12) Müller, S.; Liu, Y.; Vishnuvarthan, M.; Sun, X.; van Veen, A. C.; Haller, G. L.; Sanchez-Sanchez, M.; Lercher, J. A. Coke Formation and Deactivation Pathways on H-ZSM-5 in the Conversion of Methanol to Olefins. *J. Catal.* **2015**, *325*, 48−59.
(13) Guisnet, M.; Costa, L.; Ribeiro, F. R. Prevention of Zeolite Deactivation by Coking. *J. Mol. Catal. A: Chem.* **2009**, *305*, 69−83.
(14) Dejaifve, P.; Védrine, J. C.; Bolis, V.; Derouane, E. Reaction Pathways for the Conversion of Methanol and Olefins on H-ZSM-5 Zeolite. *J. Catal.* **1980**, *63*, 331−345.
(15) Wang, S.; Chen, Y.-Y.; Wei, Z.; Qin, Z.; Ma, H.; Dong, M.; Li, J.; Fan, W.; Wang, J. Polymethylbenzene or Alkene Cycle? Theoretical Study on Their Contribution to the Process of Methanol to Olefins over H-ZSM-5 Zeolite. *J. Phys. Chem. C* **2015**, *119*, 28482−28498.
(16) Wang, C.-M.; Wang, Y.-D.; Liu, H.-X.; Yang, G.; Du, Y.-J.; Xie, Z.-K. Aromatic-based Hydrocarbon Pool Mechanism for Methanol-to-olefins Conversion in H-SAPO-18: A Van Der Waals Density Functional Study. *Chin. J. Catal.* **2015**, *36*, 1573−1579.
(17) Hwang, A.; Prieto-Centurion, D.; Bhan, A. Isotopic Tracer Studies of Methanol-to-olefins Conversion over HSAPO-34: The Role of the Olefins-based Catalytic Cycle. *J. Catal.* **2016**, *337*, 52−56.
(18) Sun, X.; Mueller, S.; Shi, H.; Haller, G. L.; Sanchez-Sanchez, M.; van Veen, A. C.; Lercher, J. A. On the Impact of Co-feeding Aromatics and Olefins for the Methanol-to-olefins Reaction on HZSM-5. *J. Catal.* **2014**, *314*, 21−31.
(19) Wang, C.-M.; Wang, Y.-D.; Xie, Z.-K. Verification of the Dual Cycle Mechanism for Methanol-to-olefin Conversion in HSAPO-34: a Methylbenzene-based Cycle from DFT Calculations. *Catal. Sci. Technol.* **2014**, *4*, 2631−2638.
(20) Hill, I. M.; Hashimi, S. A.; Bhan, A. Kinetics and Mechanism of Olefin Methylation Reactions on Zeolites. *J. Catal.* **2012**, *285*, 115−123.
(21) Svelle, S.; Joensen, F.; Nerlov, J.; Olsbye, U.; Lillerud, K.-P.; Kolboe, S.; Bjørgen, M. Conversion of Methanol into Hydrocarbons over Zeolite H-ZSM-5: Ethene Formation Is Mechanistically Separated from the Formation of Higher Alkenes. *J. Am. Chem. Soc.* **2006**, *128*, 14770−14771.
(22) Lukyanov, D. B.; Gnep, N. S.; Guisnet, M. R. Kinetic Modeling of Ethene and Propene Aromatization over HZSM-5 and GaHZSM-5. *Ind. Eng. Chem. Res.* **1994**, *33*, 223−234.
(23) Lukyanov, D. B.; Gnep, N. S.; Guisnet, M. R. Kinetic Modeling of Propane Aromatization Reaction over HZSM-5 and GaHZSM-5. *Ind. Eng. Chem. Res.* **1995**, *34*, 516−523.
(24) Wilhelmsson, B. Formaldehyde. *Rhinology* **1985**, *23*, 128−129.
(25) Wang, S.; Agirrezabal-Telleria, I.; Bhan, A.; Simonetti, D.; Takanabe, K.; Iglesia, E. Catalytic Routes to Fuels from C1 and Oxygenate Molecules. *Faraday Discuss.* **2017**, *197*, 9−39.
(26) Hwang, A.; Kumar, M.; Rimer, J. D.; Bhan, A. Implications of Methanol Disproportionation on Catalyst Lifetime for Methanol-to-olefins Conversion by HSSZ-13. *J. Catal.* **2017**, *346*, 154−160.
(27) Joshi, Y. V.; Thomson, K. T. Brønsted Acid Catalyzed Cyclization of C7 and C8 Dienes in HZSM-5: A Hybrid QM/MM Study and Comparison with C6 Diene Cyclization. *J. Phys. Chem. C* **2008**, *112*, 12825−12833.
(28) Joshi, Y. V.; Bhan, A.; Thomson, K. T. DFT-Based Reaction Pathway Analysis of Hexadiene Cyclization via Carbenium Ion Intermediates: Mechanistic Study of Light Alkane Aromatization Catalysis. *J. Phys. Chem. B* **2004**, *108*, 971−980.
(29) Joshi, Y.; Thomson, K. Embedded Cluster (QM/MM) Investigation of C6 Diene Cyclization in HZSM-5. *J. Catal.* **2005**, *230*, 440−463.
(30) Arstad, B.; Nicholas, J. B.; Haw, J. F. Theoretical Study of the Methylbenzene Side-chain Hydrocarbon Pool Mechanism in Methanol to Olefin Catalysis. *J. Am. Chem. Soc.* **2004**, *126*, 2991−3001.
(31) Wang, C.-M.; Wang, Y.-D.; Xie, Z.-K.; Liu, Z.-P. Methanol to Olefin Conversion on HSAPO-34 Zeolite from Periodic Density Functional Theory Calculations: A Complete Cycle of Side Chain Hydrocarbon Pool Mechanism. *J. Phys. Chem. C* **2009**, *113*, 4584−4591.
(32) Ilias, S.; Bhan, A. The Mechanism of Aromatic Dealkylation in Methanol-to-hydrocarbons Conversion on H-ZSM-5: What Are the Aromatic Precursors to Light Olefins? *J. Catal.* **2014**, *311*, 6−16.
(33) Martinez-Espin, J. S.; Mortén, M.; Janssens, T. V. W.; Svelle, S.; Beato, P.; Olsbye, U. New Insights into Catalyst Deactivation and Product Distribution of Zeolites in the Methanol-to-hydrocarbons (MTH) Reaction with Methanol and Dimethyl Ether Feeds. *Catal. Sci. Technol.* **2017**, *7*, 2700−2716.

https://dx.doi.org/10.1021/acscatal.9b04529
ACS Catal. 2020, 10, 4593−4607

(34) Dai, W.; Wu, G.; Li, L.; Guan, N.; Hunger, M. Mechanisms of the Deactivation of SAPO-34 Materials with Different Crystal Sizes Applied as MTO Catalysts. *ACS Catal.* **2013**, *3*, 588−596.
(35) Bjørgen, M.; Olsbye, U.; Kolboe, S. Coke Precursor Formation and Zeolite Deactivation: Mechanistic Insights from Hexamethylbenzene Conversion. *J. Catal.* **2003**, *215*, 30−44.
(36) Bjørgen, M.; Akyalcin, S.; Olsbye, U.; Benard, S.; Kolboe, S.; Svelle, S. Methanol to Hydrocarbons over Large Cavity Zeolites: Toward a Unified Description of Catalyst Deactivation and the Reaction Mechanism. *J. Catal.* **2010**, *275*, 170−180.
(37) Arora, S. S.; Nieskens, D. L. S.; Malek, A.; Bhan, A. Lifetime Improvement in Methanol-to-olefins Catalysis over Chabazite Materials by High-pressure H_2 Co-feeds. *Nat. Catal.* **2018**, *1*, 666−672.
(38) Zhao, X.; Li, J.; Tian, P.; Wang, L.; Li, X.; Lin, S.; Guo, X.; Liu, Z. Achieving a Super-long Lifetime in the Zeolite-catalyzed MTO Reaction Under High Pressure: Synergistic Effect of Hydrogen and Water. *ACS Catal.* **2019**, *9*, 3017−3025.
(39) Arora, S. S.; Shi, Z.; Bhan, A. A Mechanistic Basis for Effects of High-pressure H_2 Co-feeds on Methanol-to-hydrocarbons Catalysis over Zeolites. *ACS Catal.* **2019**, 6407.
(40) Wristers, J. Strong Acid-catalyzed Hydrogenation of Aromatics. *J. Am. Chem. Soc.* **1975**, *97*, 4312−4316.
(41) Siria, J. C.; Duran, M.; Lledos, A.; Bertran, J. Acid-catalyzed Hydrogenation of Olefins. A Theoretical Study of the Hydrogen Fluoride and H3O+ Catalyzed Hydrogenation of Ethylene. *J. Am. Chem. Soc.* **1987**, *109*, 7623−7629.
(42) Senger, S.; Radom, L. Zeolites as Transition-Metal-Free Hydrogenation Catalysts: A Theoretical Mechanistic Study. *J. Am. Chem. Soc.* **2000**, *122*, 2613−2620.
(43) Janda, A.; Bell, A. T. Effects of Si/Al Ratio on the Distribution of Framework Al and on the Rates of Alkane Monomolecular Cracking and Dehydrogenation in H-MFI. *J. Am. Chem. Soc.* **2013**, *135*, 19193−19207.
(44) Narbeshuber, T. F.; Brait, A.; Seshan, K.; Lercher, J. A. Dehydrogenation of Light Alkanes over Zeolites. *J. Catal.* **1997**, *172*, 127−136.
(45) Van der Mynsbrugge, J.; Janda, A.; Mallikarjun Sharada, S.; Lin, L.-C.; Van Speybroeck, V.; Head-Gordon, M.; Bell, A. T. Theoretical Analysis of the Influence of Pore Geometry on Monomolecular Cracking and Dehydrogenation of *n*-Butane in Brønsted Acidic Zeolites. *ACS Catal.* **2017**, *7*, 2685−2697.
(46) Mallikarjun Sharada, S.; Zimmerman, P. M.; Bell, A. T.; Head-Gordon, M. Insights into the Kinetics of Cracking and Dehydrogenation Reactions of Light Alkanes in H-MFI. *J. Phys. Chem. C* **2013**, *117*, 12600−12611.
(47) Liu, Y.; Kirchberger, F. M.; Müller, S.; Eder, M.; Tonigold, M.; Sanchez-Sanchez, M.; Lercher, J. A. Critical Role of Formaldehyde During Methanol Conversion to Hydrocarbons. *Nat. Commun.* **2019**, *10*, No. 1462.
(48) Müller, S.; Liu, Y.; Kirchberger, F. M.; Tonigold, M.; Sanchez-Sanchez, M.; Lercher, J. A. Hydrogen Transfer Pathways During Zeolite Catalyzed Methanol Conversion to Hydrocarbons. *J. Am. Chem. Soc.* **2016**, *138*, 15994−16003.
(49) Hwang, A.; Bhan, A. Bifunctional Strategy Coupling Y_2 O_3 -Catalyzed Alkanal Decomposition with Methanol-to-Olefins Catalysis for Enhanced Lifetime. *ACS Catal.* **2017**, *7*, 4417−4422.
(50) Kresse, G.; Hafner, J. *Ab Initio* Molecular Dynamics for Liquid Metals. *Phys. Rev. B* **1993**, *47*, 558−561.
(51) Kresse, G.; Hafner, J. Ab Initio Molecular-dynamics Simulation of the Liquid-metal-amorphous-semiconductor Transition in Germanium. *Phys. Rev. B: Condens. Matter* **1994**, *49*, 14251−14269.
(52) Kresse, G.; Furthmüller, J. Efficient Iterative Schemes for Ab Initio Total-energy Calculations Using a Plane-wave Basis Set. *Phys. Rev. B: Condens. Matter* **1996**, *54*, 11169−11186.
(53) Kresse, G.; Furthmüller, J. Efficiency of Ab-initio Total Energy Calculations for Metals and Semiconductors Using a Plane-wave Basis Set. *Comput. Mater. Sci.* **1996**, *6*, 15−50.
(54) Kravchenko, P.; Plaisance, C.; Hibbitts, D. A New Computational Interface for Catalysis. *ChemRxiv* **2019**, 1−19.
(55) Perdew, J. P.; Burke, K.; Ernzerhof, M. Generalized Gradient Approximation Made Simple. *Phys. Rev. Lett.* **1996**, *77*, 3865−3868.
(56) Zhang, Y.; Yang, W. Comment on "Generalized Gradient Approximation Made Simple. *Phys. Rev. Lett.* **1998**, *80*, 890−890.
(57) Hammer, B.; Hansen, L. B.; Nørskov, J. K. Improved Adsorption Energetics Within Density-functional Theory Using Revised Perdew-Burke-Ernzerhof Functionals. *Phys. Rev. B* **1999**, *59*, 7413−7421.
(58) Grimme, S.; Ehrlich, S.; Goerigk, L. Effect of the Damping Function in Dispersion Corrected Density Functional Theory. *J. Comput. Chem.* **2011**, *32*, 1456−1465.
(59) Schröder, H.; Creon, A.; Schwabe, T. Reformulation of the D3(Becke-Johnson) Dispersion Correction Without Resorting to Higher Than C_6 Dispersion Coefficients. *J. Chem. Theory Comput.* **2015**, *11*, 3163−3170.
(60) Grimme, S.; Antony, J.; Ehrlich, S.; Krieg, H. A Consistent and Accurate Ab Initio Parametrization of Density Functional Dispersion Correction (DFT-D) for the 94 Elements H-Pu. *J. Chem. Phys.* **2010**, *132*, No. 154104.
(61) Monkhorst, H. J.; Pack, J. D. Special Points for Brillouin-zone Integrations. *Phys. Rev. B* **1976**, *13*, 5188−5192.
(62) Goncalves, T. J.; Plessow, P. N.; Studt, F. On the Accuracy of Density Functional Theory in Zeolite Catalysis. *ChemCatChem* **2019**, 4368.
(63) van Koningsveld, H. High-temperature (350 K) Orthorhombic Framework Structure of Zeolite H-ZSM-5. *Acta Crystallogr., Sect. B: Struct. Sci.* **1990**, *46*, 731−735.
(64) Hoffman, A.; DeLuca, M.; Hibbitts, D. Restructuring of MFI Framework Zeolite Models and Their Associated Artifacts in Density Functional Theory Calculations. *J. Phys. Chem. C* **2019**, *123*, 6572−6585.
(65) Ghorbanpour, A.; Rimer, J. D.; Grabow, L. C. Computational Assessment of the Dominant Factors Governing the Mechanism of Methanol Dehydration over H-ZSM-5 with Heterogeneous Aluminum Distribution. *ACS Catal.* **2016**, *6*, 2287−2298.
(66) DeLuca, M.; Kravchenko, P.; Hoffman, A.; Hibbitts, D. Mechanism and Kinetics of Methylating C_6 $-C_{12}$ Methylbenzenes with Methanol and Dimethyl Ether in H-MFI Zeolites. *ACS Catal.* **2019**, *9*, 6444−6460.
(67) Jónsson, H.; Mills, G.; Jacobsen, K. W. Nudged Elastic Band Method for Finding Minimum Energy Paths of Transitions. In *Classical and Quantum Dynamics in Condensed Phase Simulations*; Berne, B. J.; Ciccotti, G.; Coker, D. F., Eds.; World Scientific, 1998; pp 385−404.
(68) Henkelman, G.; Jónsson, H. A Dimer Method for Finding Saddle Points on High Dimensional Potential Surfaces Using Only First Derivatives. *J. Chem. Phys.* **1999**, *111*, 7010−7022.
(69) Martinez-Espin, J. S.; De Wispelaere, K.; Westgård Erichsen, M.; Svelle, S.; Janssens, T. V. W.; Van Speybroeck, V.; Beato, P.; Olsbye, U. Benzene Co-reaction with Methanol and Dimethyl Ether over Zeolite and Zeotype Catalysts: Evidence of Parallel Reaction Paths to Toluene and Diphenylmethane. *J. Catal.* **2017**, *349*, 136−148.
(70) Kistiakowsky, G. B.; Nickle, A. G. Ethane-ethylene and Propane-propylene Equilibria. *Discuss. Faraday Soc.* **1951**, *10*, 175.
(71) Kistiakowsky, G. B.; Romeyn, H.; Ruhoff, J. R.; Smith, H. A.; Vaughan, W. E. Heats of Organic Reactions. I. the Apparatus and the Heat of Hydrogenation of Ethylene. *J. Am. Chem. Soc.* **1935**, *57*, 65−75.
(72) Chu, Y.; Han, B.; Fang, H.; Zheng, A.; Deng, F. Influence of Acid Strength on the Reactivity of Alkane Activation on Solid Acid Catalysts: A Theoretical Calculation Study. *Microporous Mesoporous Mater.* **2012**, *151*, 241−249.
(73) Martínez-Espín, J. S.; De Wispelaere, K.; Janssens, T. V. W.; Svelle, S.; Lillerud, K. P.; Beato, P.; Van Speybroeck, V.; Olsbye, U. Hydrogen Transfer Versus Methylation: On the Genesis of Aromatics

https://dx.doi.org/10.1021/acscatal.9b04529
ACS Catal. 2020, 10, 4593−4607

Formation in the Methanol-To-Hydrocarbons Reaction over H-ZSM-5. *ACS Catal.* **2017**, *7*, 5773−5780.
(74) Sun, X.; Mueller, S.; Liu, Y.; Shi, H.; Haller, G. L.; Sanchez-Sanchez, M.; van Veen, A. C.; Lercher, J. A. On Reaction Pathways in the Conversion of Methanol to Hydrocarbons on HZSM-5. *J. Catal.* **2014**, *317*, 185−197.
(75) Jones, A. J.; Iglesia, E. The Strength of Brønsted Acid Sites in Microporous Aluminosilicates. *ACS Catal.* **2015**, *5*, 5741−5755.
(76) Brogaard, R. Y.; Wang, C.-M.; Studt, F. Methanol−Alkene Reactions in Zeotype Acid Catalysts: Insights from a Descriptor-Based Approach and Microkinetic Modeling. *ACS Catal.* **2014**, *4*, 4504−4509.
(77) Wang, C.-M.; Brogaard, R. Y.; Weckhuysen, B. M.; Nørskov, J. K.; Studt, F. Reactivity Descriptor in Solid Acid Catalysis: Predicting Turnover Frequencies for Propene Methylation in Zeotypes. *J. Phys. Chem. Lett.* **2014**, *5*, 1516−1521.
(78) Plessow, P. N.; Studt, F. Theoretical Insights into the Effect of the Framework on the Initiation Mechanism of the MTO Process. *Catal. Lett.* **2018**, 1246.
(79) Wang, C.-M.; Wang, Y.-D.; Du, Y.-J.; Yang, G.; Xie, Z.-K. Similarities and Differences Between Aromatic-based and Olefin-based Cycles in H-SAPO-34 and H-SSZ-13 for Methanol-to-olefins Conversion: Insights from Energetic Span Model. *Catal. Sci. Technol.* **2015**, *5*, 4354−4364.
(80) Towns, J.; Cockerill, T.; Dahan, M.; Foster, I.; Gaither, K.; Grimshaw, A.; Hazlewood, V.; Lathrop, S.; Lifka, D.; Peterson, G. D.; Roskies, R.; Scott, J. R.; Wilkens-Diehr, N. XSEDE: Accelerating Scientific Discovery. *Comput. Sci. Eng.* **2014**, *16*, 62−74.

https://dx.doi.org/10.1021/acscatal.9b04529
ACS Catal. 2020, 10, 4593−4607